ACS NANO

www.acsnano.org

ARTICLE

Mechanically Robust, Superlubricating and Antifouling Bilayer Nanocoating for Micro-Bioimplants via a Dual-Function Metal Coordination Approach

Li Xiang, Yuhao Zhang, Ziqian Zhao, Yi Tao, Wenda Wang, Jifang Liu, Yunfei Chen, Jinyang Jiang,* Jiawen Zhang,* and Hongbo Zeng*

Cite This: https://doi.org/10.1021/acsnano.4c13800

Read Online

ACCESS | Metrics & More | Article Recommendations | Supporting Information

ABSTRACT: **Nanometer-thick ultrathin coatings with superior mechanical strength and desirable lubricating and antifouling performance are critical for the miniaturization of implantable medical devices. However, integrating these properties at the nanoscale remains challenging due to the inherent trade-off between mechanical strength and hydration as well as limitations in coating thickness. In this work, we address these challenges by employing dual-function metal coordination to construct a ∼25 nm thick bilayer structure. Contact mechanics and interfacial molecular force measurements confirm the dual role of vanadium (V^{III}) ions in forming this bilayer: V^{III} ions bridge the ligand sites to reinforce the protein bottom layer, and simultaneously anchor the end blocks of the designed ABA triblock hydrophilic polymers to form a hydrated, looping top layer. This V^{III}-enabled structure demonstrates remarkable load-bearing capacity and lubricating performance (i.e., friction coefficient μ on the order of 10^{-3} over 100 cycles under ∼10 MPa), while it also exhibits excellent resistance to biofouling in complex biological fluids. This work presents a useful strategy for integrating seemingly incompatible properties into ultrathin coatings, offering the potential for customizing multifunctional surfaces for micro-devices/machines toward bioengineering applications.**

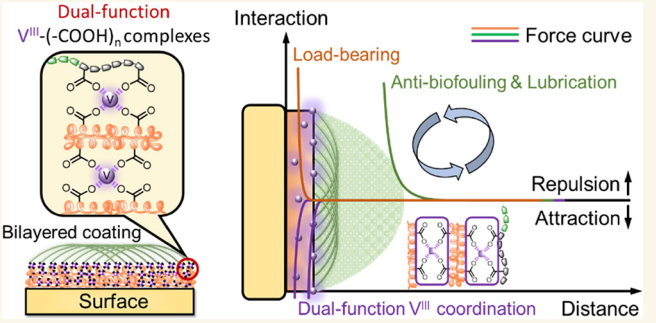

KEYWORDS: *ultrathin bilayer structure, dual-function metal coordination, interfacial strengthening, intermolecular interactions, microbioimplants*

Advanced implantable medical devices (IMDs), such as articular implants and vascular catheters, require elaborate surface decoration for long-term proper function in physiological environments.[1−7] A prominent example is the hydrophilic polymeric coating on artificial blood vessels for vascular replacement.[8−11] The functionalized vessel wall must endure mechanical stresses from continuous blood pressure while remaining strongly hydrated to resist biofouling (e.g., protein adsorption) and minimize shear forces from flowing blood, which reduces the risk of adverse effects such as plasma coagulation and thrombus formation.[12] To meet these stringent requirements, considerable efforts have been dedicated to developing functional coatings that integrate high mechanical strength with superior antifouling and lubricating properties.[13−16] Introducing cross-links into the polymer coating network, such as physical interaction,[17,18] double-bond addition[19,20] and metal−ligand complexation,[21,22] is considered as the most effective and accessible approach for the mechanical robustness of the coating system.[20] Yet, high cross-linking density would inevitably hamper the movement of polymer chains and the water diffusion in the polymer network, weakening the binding of water molecules with polymers to lower the coating hydration capability, which dramatically weakens their antifouling and lubricating performance.[23,24]

Received: September 30, 2024
Revised: December 10, 2024
Accepted: December 17, 2024

Recently, polymeric coatings with a bilayer structure, comprising a mechanically robust bottom layer and hydrated top layer, have been developed to overcome this trade-off, endowing many bioimplants with as-required surface functionalities for practical applications.[25,26] In such systems, the bottom layers are usually fabricated as hundreds of micrometer-thick to (1) provide sufficient mechanical support and (2) facilitate deep interpenetration and entanglement (tens of micrometers) with the top layer, ensuring interface robustness. While effective for large-scale bioimplants, these coatings are less suitable for micro/nano-scale devices due to dimensional incompatibility. For instance, applying a hundred-micrometer-thick coating to the inner wall of a small-diameter artificial blood vessel (SDABV) (internal diameters D_{inner} < 1 mm) would drastically reduce the vessel's diameter, severely compromising the function of vascular graft.[27,28] Thus, achieving a nanometer-thick coating that simultaneously offers high mechanical strength along with excellent antifouling and lubricating properties is crucial yet remains a challenge. We propose that an ideal nanoscale bilayer coating should exhibit two key characteristics: (1) a bottom layer with nanometer-scale thickness capable of providing adequate mechanical strength and (2) secure bonding that forms directly at the interface between the bottom and top layers.

In the field of mussel adhesion science, vanadium ion (V^{III}) has recently been identified as playing a critical role in mechanically reinforcing the thin byssal cuticle (thickness of ~5 μm) via metal−ligand coordination.[29,30] Despite this discovery, no work has leveraged this robust V^{III}-ligand cross-linking to develop high-performance ultrathin coating materials, which could offer a promising strategy for engineering multifunctional ultrathin hierarchical structures. Herein, we present the development of a nanoscale bilayer coating (~25 nm) by using a dual-functional metal coordination strategy that combines high mechanical strength with strong hydration capacity. This hierarchical coating consists of a bovine serum albumin (BSA) protein cushion as the bottom layer and a designed ABA triblock hydrophilic polymer as the top layer. The V^{III} ions play a dual role in reinforcing the mechanical strength of the protein bottom layer. On one hand, V^{III} ions form coordination cross-links within the protein network with high density, on the other hand, V^{III} ions anchor the two end blocks of ABA polymers to the bottom layer, forming a looping top layer. The coordination-enhanced structural robustness, coupled with the hydrated loop conformation of the top layer, enables the bilayer coating to maintain long-lasting superlubricity under high pressure (~10 MPa) and resist the adsorption of various biofoulants under a model physiological environment. As a proof-of-concept, the potential application of this bilayer coating is further demonstrated in an SDABV (internal diameter of ~0.79 mm). This coating significantly enhances the antibiofouling and interfacial lubricating properties under blood pressure, as demonstrated by an in vitro blood circulation test. This ultrathin, hierarchical, and multifunctional coating holds promise in surface engineering in various microscale bioimplants for biomedical applications.

RESULTS AND DICUSSION

The ultrathin bilayer coating was constructed via a two-step surface modification using a simple dipping method, as depicted in Figure 1A. BSA proteins bound with carboxyl groups (−COOH) were used for the first-step surface modification. The diverse functional groups on BSA enabled

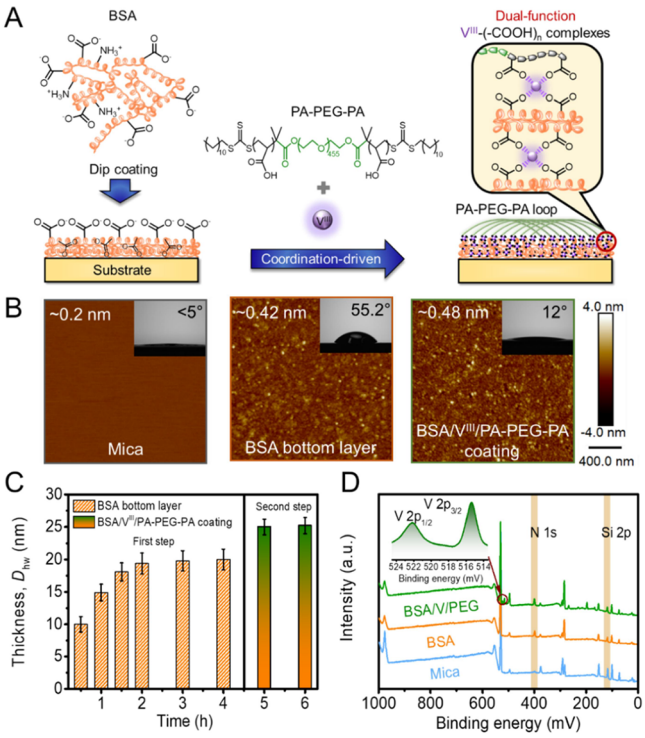

Figure 1. Bilayer coating preparation and characterization. (A) Two-step surface functionalization through a dual-functional metal coordination strategy. (B) Atomic force microscopy (AFM) topographic images of bare mica, the bovine serum albumin (BSA) bottom layer, and the poly(acrylic acid)-*b*-poly(ethylene glycol)-*b*-poly(acrylic acid) (PA−PEG-PA) top layer anchored to the bottom layer by vanadium ion (V^{III}) (viz., BSA/V^{III}/PA−PEG-PA coating). (C) Coating thickness variation over the deposition time. (D) X-ray photoelectron spectra (XPS) of bare mica, the BSA bottom layer, and the BSA/V^{III}/PA−PEG-PA coating. The inset displays a high-resolution V^{III} spectrum.

their robust adhesion on the target surface to form the bottom layer via multiple molecular interactions.[31,32] An ABA triblock copolymer, namely, poly(acrylic acid)-*b*-poly(ethylene glycol)-*b*-poly(acrylic acid) (PA−PEG-PA), was designed for the second-step surface modification (polymer characterization shown in Supporting Information (SI) Figure S1). Since both terminal "A" blocks and BSA protein contain −COOHs as ligand sites, introducing V^{III} ions could anchor the PA−PEG-PA to the BSA protein layer through metal−ligand coordination,[33] rendering the hydrophilic "B" midblock to adopt the loop conformation as the top layer. In addition, V^{III} ions could also diffuse into the bottom layer, strengthening the protein network by forming the V^{III}−COOH complex between BSA chains.[34] The as-prepared bilayer is denoted as the BSA/V^{III}/PA−PEG-PA coating.

Atomic force microscopy (AFM) topographic imaging and water contact angle (WCA) test exhibit obvious changes in surface morphology and hydrophilicity after the surface modification (Figure 1B). BSA proteins were found to adsorb on the mica substrate to form a compact and uniform bottom layer. The increased surface WCA compared with that of bare mica results from the hydrophobic parts in BSA. PA−PEG-PA polymers were found to form a more densely packed layer overlaying on the BSA-coated surface, which resulted in a decreased WCA due to the introduced hydrophilic PEG midblock.[35] The thickness of the BSA/V^{III}/PA−PEG-PA

https://doi.org/10.1021/acsnano.4c13800
ACS Nano XXXX, XXX, XXX−XXX

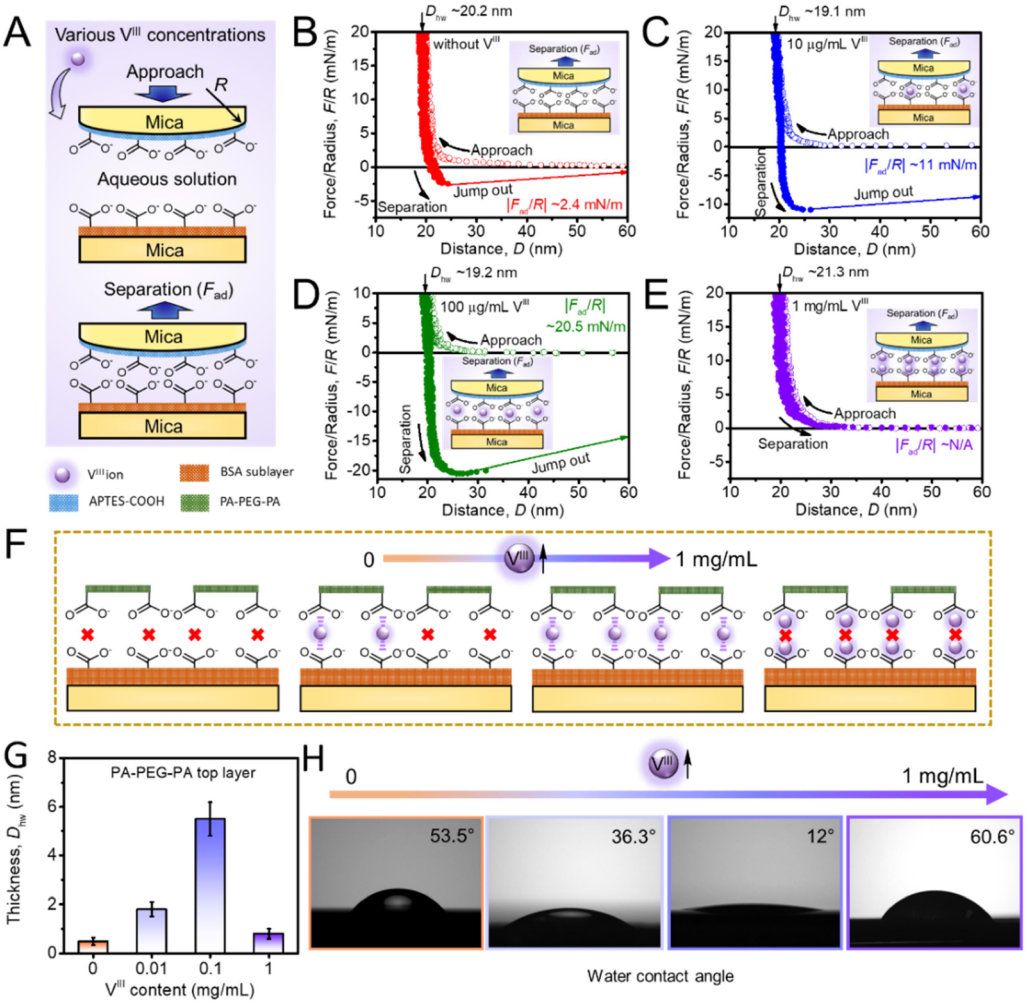

Figure 2. V^{III} coordination-mediated BSA/V^{III}/PA−PEG-PA bilayer interfacial bridging. (A) Schematics of interfacial force measurement using a surface forces apparatus (SFA). Two opposing curved mica surfaces (radius R) modified by BSA proteins and carboxyl groups (−COOH) first approached and contacted with each other followed by separation to measure the adhesion force (F_{ad}). Normalized force−distance profiles and adhesion were measured between BSA-coated and −COOH group-modified mica surfaces in PBS aqueous buffer (150 mM, pH 7.4) with the introduced V^{III} concentrations of (B) 0, (C) 0.01, (D) 0.1, and (E) 1 mg/mL. (F) Diagram of V^{III}-mediated −COOH coordination interaction transforming from multi- to mono- complexation. Influence of introduced V^{III} concentration on (G) the thickness and (H) the water contact angle (WCA) of the PA−PEG-PA top layer formed on the BSA bottom layer.

bilayer was measured as ∼25 nm by using a surface forces apparatus (SFA, SI Figure S2), including a ∼20 nm bottom layer and a ∼5 nm top layer (Figure 1C). A strong vanadium peak was detected on the bilayer coating by X-ray photoelectron spectra (XPS) analysis, as shown in Figure 1D. Considering that thoroughly rinsing the coating would remove unbound and/or loosely bound V^{III} ions, the V^{III} ions remaining on the surface are supposed to actively participate in constructing the BSA/V^{III}/PA−PEG-PA coating.[29]

To elucidate the critical role of V^{III} in integrating the BSA bottom layer and the PA−PEG-PA top layer, the interfacial interactions between BSA-coated and −COOH group-modified mica surfaces were quantitatively investigated in PBS aqueous buffer (150 mM, pH 7.4) with varied V^{III} concentrations using SFA (Figure 2A). Here, the −COOH groups grafted on the mica surface were used as the model groups for the terminal "A" blocks of PA−PEG-PA polymers. Without V^{III}, a weak adhesion of F_{ad}/R ∼ 2.4 mN/m was detected between the BSA layer and the −COOH-modified mica surface (Figure 2B). Although both surfaces are negatively charged at pH 7.4,[36] this measured adhesion could be attributed to the shortened Debye length of electric double layer (EDL) repulsion under the high salinity condition of PBS, allowing for short-range attractive interactions such as hydrogen bonding formed at the interface.[37] When 0.01 and 0.1 mg/mL V^{III} ions were introduced (Figure 2C,D), F_{ad}/R significantly enhanced to ∼11 and ∼20.5 mN/m, respectively, manifesting the pivotal role of V^{III} in strengthening the interface of the BSA/V^{III}/PA−PEG-PA bilayer. Further increasing the concentration of V^{III} ions to 1 mg/mL drastically converted the adhesion into a pure repulsion (Figure 2E). This V^{III} concentration-dependent interaction evolution can be reasonably interpreted by previously reported trivalent metal ion-mediated coordination behavior.[22] As illustrated in Figure 2F, a properly increased V^{III} concentration could bring more V^{III} ions to bridge the interface through bis- and/or multiple complexations with −COOH groups at two opposing surfaces, whereas excess V^{III} would abolish this bridging effect by forming a mono metal−ligand complex. It is worth noting that the V^{III} concentration-dependent adhesion variation followed the same trend of the top layer thickness and surface hydrophilicity after depositing PA−PEG-PA

https://doi.org/10.1021/acsnano.4c13800
ACS Nano XXXX, XXX, XXX−XXX

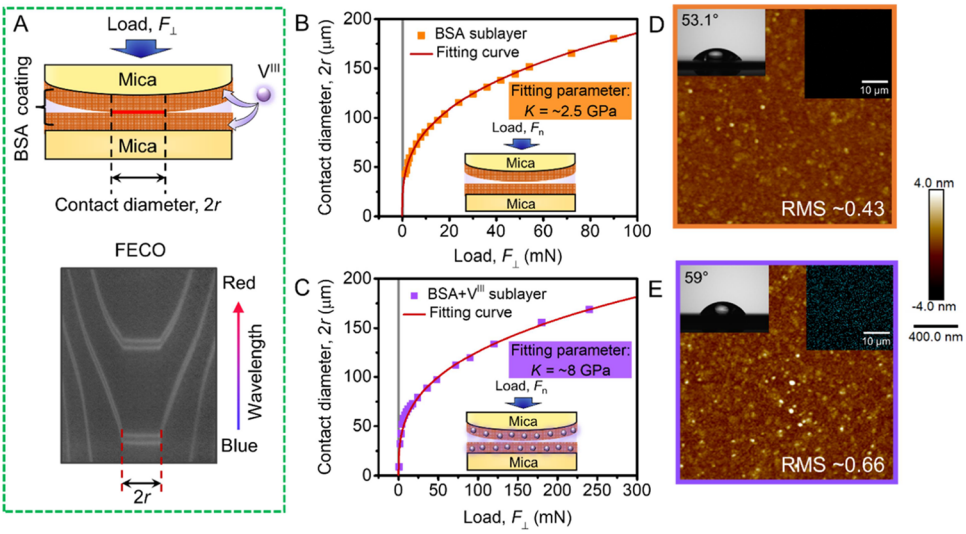

Figure 3. Investigation on the mechanical property of the BSA bottom layer with/without V^{III} via contact mechanics measurements. (A) Schematics of two symmetric BSA layers coated on mica in intimate contact under an external load of $F_\perp$ (upper) and a typical fringes of equal chromatic order (FECO) pattern (lower). Hertzian plot of (B) two weakly adhering BSA protein layers and (C) two nonadhering V^{III}-incorporated BSA layers in PBS aqueous buffer (150 mM, pH 7.4). AFM topographic images of the as-formed BSA layers on mica surfaces (D) with and (E) without the introduction of V^{III}. The insets display WCAs of the sessile water droplets and energy-dispersive spectroscopy (EDS) element mapping of V on BSA and V^{III}-incorporated BSA layers.

polymers on the BSA bottom layer under a series of V^{III} concentrations (Figure 2G,H). The slightly higher WCA of BSA coating after being treated by PA−PEG-PA and 1 mg/mL V^{III} solution compared with that being treated by only PA−PEG-PA is mainly due to the following reasons. First, at the concentration of 1 mg/mL, the V^{III} ions were excessively introduced to the system. The binding sites (i.e., carboxyl groups) on both BSA and PA−PEG-PA were respectively occupied by V^{III} ions through forming a mono metal−ligand complex. Consequently, the V^{III}-induced bridging between BSA and PA−PEG-PA was abolished, impeding the hydrophilic PA−PEG-PA polymer from anchoring on the BSA coating. Second, the formation of coordination bonds between V^{III} and hydrophilic carboxyl groups on BSA weakened the binding affinity of BSA with water molecules, resulting in the increased hydrophobicity of the BSA coating. These two effects play a synergistic role in increasing the contact water of the BSA coating after being treated with PA−PEG-PA and 1 mg/mL V^{III} solution. The consistency of the V^{III} concentration-dependent adhesion behavior, top layer thickness, and surface wettability evidenced the indispensable contribution of V^{III}-based bis- and/or multi-coordination in constructing the BSA/V^{III}/PA−PEG-PA bilayer.[38,39]

In addition to realizing the interface bridging of the bilayer, the role of V^{III} ions in improving the mechanical strength of the BSA bottom layer was assessed through contact mechanics measurements. Figure 3A shows the typical experimental setup of contact mechanics tests between two BSA-coated or two V^{III}-incorporated BSA-coated surfaces by using SFA. When two surfaces were brought into contact, the contact diameter $2r$ could be determined from the flat region in the wavelength spectrum of FECO fringes.[40] For the intimate contact of two BSA-coated surfaces and two V^{III}-incorporated BSA-coated surfaces, both of their contact diameters increased with the elevation of the external load $F_\perp$, as shown in Figure 3B,C. However, to achieve the same $2r$, a much higher normal load was required to apply on V^{III}-incorporated BSA layers than on BSA layers. Given that the surface morphology of the BSA layer and V^{III}-incorporated BSA layer was similar to comparable surface roughness (Figure 3D,E), such loading disparity is more likely because of the difference in the mechanical strength of the protein network rather than surface structure. Typical SFA-measured force−distance curves determined a weak adhesion of $F_{ad} \sim 1.6$ mN (i.e., $F_{ad} \ll F_\perp$) between two BSA layers and no adhesion force between two V^{III}-incorporated BSA layers after a contact time of 10 min (SI Figure S3). Thus, a Hertzian model was utilized to analyze the loading curves in Figure 3B,C to estimate the effective elastic modulus of BSA-coated and V^{III}-incorporated BSA-coated mica substrates.[37]

$$r^3 = \frac{R}{K} F_\perp \tag{1}$$

where r is the radius of the flattened contact area, R is the radius of curved mica glued on the cylindrical silica disk, $F_\perp$ is the external load applied to the surface, and K denotes the effective elastic modulus of the substrate material.

Fitting the loading curves with eq 1 obtained the K of ~2.5 GPa for BSA-coated mica and of ~8 GPa for V^{III}-incorporated BSA-coated mica, suggesting the significantly reinforced mechanical strength of the BSA layer after V^{III} incorporation. It is noted that the K values fitted using the Johnson−Kendall−Roberts (JKR) model are very close to the Hertzian case for the low-adhesive surfaces of BSA or V^{III}-incorporated BSA-coated mica. As the mechanical properties of a material are fundamentally governed by the intermolecular interactions between its moieties,[23,41] this extraordinary reinforcement behavior could be ascribed to the newly formed coordination bonds between the introduced V^{III} and −COOH groups on BSA to bridge the protein network. Therefore, the contact mechanics tests and the above surface force measurements corroborate the dual function of V^{III} for the structural robustness of the BSA/V^{III}/PA−PEG-PA bilayer coating.

https://doi.org/10.1021/acsnano.4c13800
ACS Nano XXXX, XXX, XXX−XXX

When being applied in complex physiological scenarios, the as-prepared BSA/V^{III}/PA−PEG-PA bilayer coating needs to possess desirable lubrication performance as a symmetric friction pair. Besides, it should also maintain reliable lubricity against biomolecules (particularly proteins) at human tissue surfaces or that are freely dispersed in blood. Given this, as illustrated in Figure 4A, the normal and frictional forces of

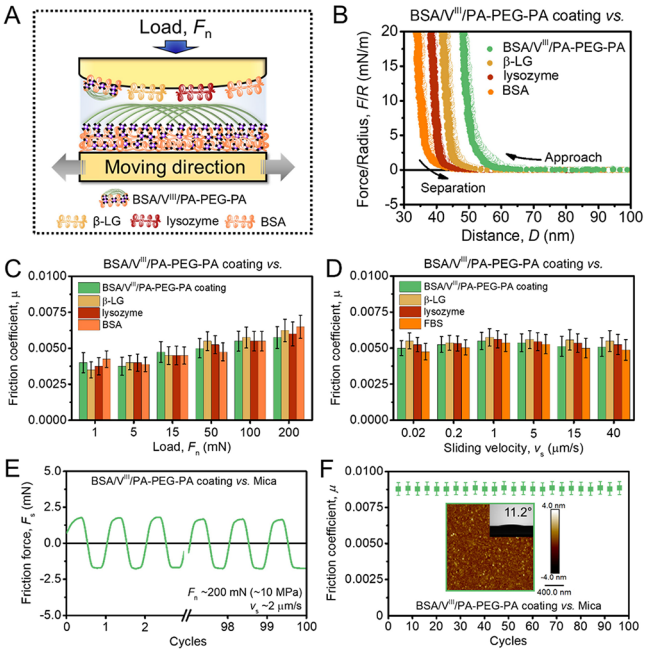

Figure 4. Evaluation of the tribological behavior of BSA/V^{III}/PA−PEG-PA bilayer coating under model physiological aqueous condition. (A) Experimental configuration of SFA friction tests between symmetric BSA/V^{III}/PA−PEG-PA bilayer coatings and between the bilayer coating and a series of biofoulant-coated surfaces in the PBS aqueous buffer (150 mM, pH 7.4). (B) Normal force curves of the interactions between two symmetric BSA/V^{III}/PA−PEG-PA bilayer coatings and between the bilayer coating and a series of biofoulant-coated surfaces. The variation of friction coefficient μ of BSA/V^{III}/PA−PEG-PA bilayer coating versus various modified surfaces under (C) different loads F_n at constant sliding velocities v_s of 2 μm/s and (D) different v_s at constant load of 50 mN. (E) and (F) Cyclic reciprocating friction tests to estimate the lubrication durability of the BSA/V^{III}/PA−PEG-PA bilayer coating under a high load of 200 mN at v_s of 2 μm/s. The inset shows the AFM topological image of contact region after 100 cycles of the reciprocating friction test.

BSA/V^{III}/PA−PEG-PA bilayer coating in PBS buffer were systematically examined in both symmetric (coating vs coating) and asymmetric (coating vs protein layer) configurations using an SFA. Common proteins including β-Lactoglobulin (β-LG), lysozyme, and BSA were selected to prepare protein layers. Figure 4B shows the normal interaction forces between BSA/V^{III}/PA−PEG-PA bilayer coatings and between BSA/V^{III}/PA−PEG-PA bilayer coating and three kinds of protein-adsorbed surfaces. For all of the cases, the forces were consistently repulsive during surface separation after the contact time of 10 min. Without the PA−PEG-PA top layer, BSA/V^{III} coating displayed strong adhesion to protein-adsorbed surfaces (SI Figure S4). Thus, the measured repulsive interaction is most likely contributed by the topmost hydrated PEG chains, generating strong steric repulsion to overwhelm any possible attractive interactions. Moreover, the pure repulsion generated by the PA−PEG-PA top layer further validated the loop conformation of the PEG midblock, because polymer bridging would be inevitable if its two end blocks were not strongly tethered onto the same substrate.[42]

The lubrication performance of the BSA/V^{III}/PA−PEG-PA bilayer coating was evaluated by measuring the friction forces of two bilayer coatings and between the bilayer coating and the protein layers under a series of applied loads and sliding velocities. Figure 4C shows the effect of a normal load on the friction behavior of the bilayer coating at a constant sliding velocity of 2 μm/s. Although elevating the load from 1 to 200 mN led to an increase in friction coefficient μ (calculated by F_s/F_n), the μ values were consistently at the order of 10^{-3} within this load range. Notably, the superlubricity ability could still be maintained under the calculated contact pressure P_{max} of ~10 MPa, comparable to the lubrication performance in tribology-related biological systems (e.g., articular cartilage),[13,43] which ensures its feasibility toward many in vivo applications associated with biotribology. In stark contrast to the dramatically increased friction coefficient (~0.1) of BSA/V^{III} coating without the PA−PEG-PA top layer (SI Figure S6), the superlubricity of BSA/V^{III}/PA−PEG-PA should be ascribed to the large excluded volume of hydrated PEG chains in aqueous media, generating strong and long-range hydration repulsion to achieve outstanding lubrication performance (Figure 4B).[7,42] Such phenomenon indicates that an effective lubricating coating, even with nanometer thickness, can significantly enhance surface lubrication ability, which could be substantiated by a previous work that subnanometer-thick lubrication film can significantly enhance surface lubricity.[44] When the load was kept at 50 mN, as shown in Figure 4D, the μ values slightly fluctuated around 0.005 in the velocity range from 0.02 to 40 μm/s. This velocity-independent lubrication behavior, which obeys Amontons' law, extends the coating's potential applicability for more complicated situations, such as a vascular graft that requires preserving its inner wall lubricity to reduce the drag force against the flowing blood at both low (artificial vein) and high (artificial artery) velocities.[45,46]

The antiwear performance of the bilayer coating was examined by conducting a reciprocating friction test of 100 sliding cycles between the bilayer coating and rigid bare mica surface at high loading conditions (F_n 200 mN, P_{max} ~ 10 MPa). As shown in Figure 4E, the friction trace exhibited a smooth transition from the linearly increased static friction force to the steady-state kinetic friction force at each back-and-forth sliding cycle. No obvious stiction friction spike was detected for the whole cyclic test. The steady-state friction force lay within the range of 1.6−1.8 mN with negligible dependence on the cycle number. The calculated μ was almost unchanged at ~0.0088 after 100 reciprocating cycles (Figure 4F), which showed a durable lubrication performance rivaling the natural hydration lubricating system. The coating morphology and hydrophilicity displayed little variation after the cyclic friction test (Figure 4F inset), indicating the retained structural integrity. This outstanding wear-resistance capacity can be attributed to the synergistic cooperation of the bilayer structure: (1) the V^{III}-strengthened BSA bottom layer provides sufficient mechanical support to bear high load; (2) the strongly hydrated PA−PEG-PA looping top layer not only significantly reduces the shearing force applied on the surface but also suppresses chain interpenetration and entanglement across two interacting surfaces under high load; (3) the as-

https://doi.org/10.1021/acsnano.4c13800
ACS Nano XXXX, XXX, XXX−XXX

formed robust interface through V^{III} coordination bridging prevents any possible interfacial fracture between the two layers.

Preventing biofouling on surfaces is another important consideration for IMDs applied in biofluidic conditions.[45−49] To investigate the antifouling property of the as-prepared bilayer coating, the adsorption behavior of three model biofoulants (i.e., β-L, lysozyme, and BSA) on bare and bilayer-coated silica sensors was monitored in real-time using the Quartz Crystal Microbalance with Dissipation (QCM-D) (Figure 5A). For the bare silica sensor, a strong negative

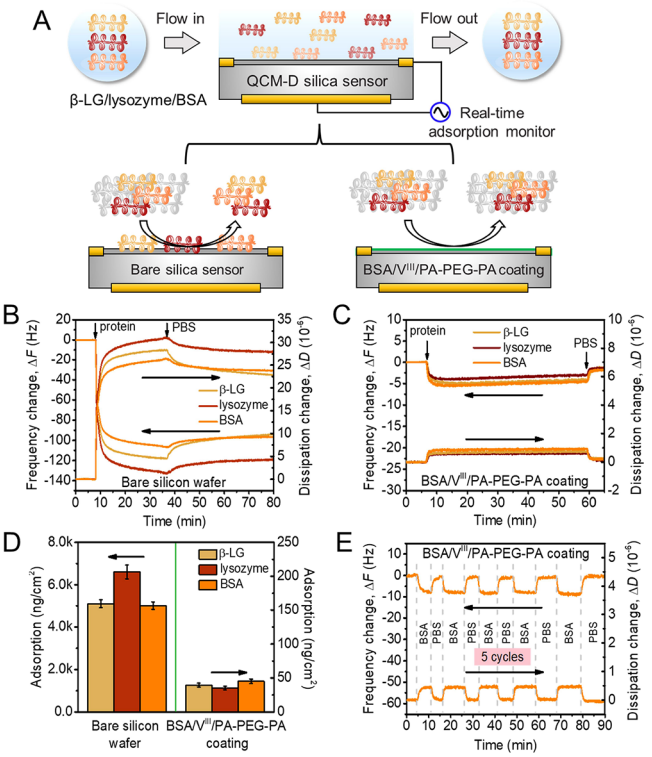

Figure 5. Real-time monitoring of the dynamic adsorption−desorption behavior of biofoulants on BSA/V^{III}/PA−PEG-PA bilayer-coated QCM-D sensors. (A) Schematics of QCM-D experimental setup for quantitatively investigating the adsorption of biofoulants on bare silica sensor and bilayer-coated silica sensor. Change in frequency and dissipation associated with the adsorption and desorption of three model biofoulants on (B) bare silica sensor and (C) bilayer-coated silica sensor. (D) Comparison of the adsorption mass of remnant biofoulants on bare and bilayer-coated silica sensors after PBS rinsing. (E) Change in frequency and dissipation with respect to the adsorption and desorption of model biofoulant on the bilayer-coated silica sensor during the alternative introduction of the BSA solution and PBS buffer.

frequency shift and positive dissipation shift were observed upon introducing biofoulant solutions into the QCM-D chamber (Figure 5B), indicating significant adsorption of biofoulants on the sensor surface. After stable frequency and dissipation curves were attained, PBS was introduced into the chamber to remove the loosely bound biofoulants. However, only slight variations in the frequency and dissipation were found after PBS rinsing, suggesting that most of the biofoulants still adsorbed on the surface and could not be removed. On the contrary, for a silica sensor coated with the bilayer, as shown in Figure 5C, the shift of frequency and dissipation curves was very limited when the biofoulant solutions were introduced. After PBS rinsing, both curves returned to almost zero level, implying that most of the adsorbed biofoulants could be readily washed off. Such adsorption−desorption behavior demonstrated the excellent foulant-repellency of the bilayer coating, which could be attributed to the highly hydrated PEG loop building an effective physical barrier to prevent the biofoulant attachment.[7] To quantify the antifouling effect, the mass of the remnant biofoulants adsorbed on two sensor surfaces after PBS rinsing was determined by fitting the QCM-D curves using the Voigt viscoelastic model (Figure 5D). In stark contrast to a significant amount (over 5000 ng/cm^2) of biofoulants remaining on the bare sensor surface, the residual mass of the biofoulants on the bilayer-coated sensor surface was almost neglectable with all the values <50 ng/cm^2. The outstanding antifouling property was further evidenced to be durable by the cyclic adsorption−desorption test shown in Figure 5E. Over 5 cycles of alternatively introducing BSA solution and PBS buffer, the adsorption−desorption of BSA on the bilayer-coated sensor was almost completely reversible, suggesting that the antifouling capacity is insusceptible with great potential for implantable biodevices toward long-term in vivo usage.[50,51]

The ultrathin BSA/V^{III}/PA−PEG-PA coating with excellent lubricating and antifouling properties is promising for surface modification on microscale IMDs. One of the most widely used microscale IMDs, as shown in Figure 6A, is SDABV (D_{inner} < 1 mm) which is utilized to replace dysfunctional arteries.[52] For newly implanted SDABV, high drag force and fibrinogen adsorption at the inner wall under high blood pressure need to be stringently avoided because both would easily induce blood clotting.[53−55] Therefore, surface functionalization, without affecting its inner diameter size, is an effective strategy to ensure the smooth flow of blood through the artificial vessel and the biofouling resistance of the inner wall. Given this, we demonstrated the capability of the as-developed ultrathin bilayer coating, which enabled the stable operation of the SDABV in a long-term in vitro blood circulation test illustrated in Figure 6B. The operation performance was estimated by comparing the variation of the blood flow rate in pristine, BSA/V^{III}-coated, and BSA/V^{III}/PA−PEG-PA-coated medical tubes under different durations of blood circulation (Figure 6C). After the circulation of 10 days, the blood flow rate in the BSA/V^{III}/PA−PEG-PA-coated medical tube was 8.83 cm/s, which retained ∼90.2% of the initial flow rate. In contrast, the flowing rate of pristine and BSA/V^{III}-coated tubes significantly reduced to 5 and 7.47 cm/s, respectively, which accounted for ∼56.3 and ∼77.3% of their initial ones.

The surface morphology of the inner wall of the three kinds of medical tubes after 10 days of operation was characterized by using SEM, as shown in Figure 6D. It was observed that large flake-like moieties fully covered the inner surface of the pristine tube; small aggregate-like moieties sparsely distributed on the BSA/V^{III}-coated inner surface; and no obvious moieties were observed on the BSA/V^{III}/PA−PEG-PA -coated inner surface. EDS mapping and line-scanning results demonstrated that strong signals and obviously increased weight percentage of C and O elements, as the main composition of biofoulants, were only detected on the inner surface of pristine and BSA/V^{III}-coated tubes rather than on the BSA/V^{III}/PA−PEG-PA-coated inner surface (Figure 6E,F). Thus, the dramatically

https://doi.org/10.1021/acsnano.4c13800
ACS Nano XXXX, XXX, XXX−XXX

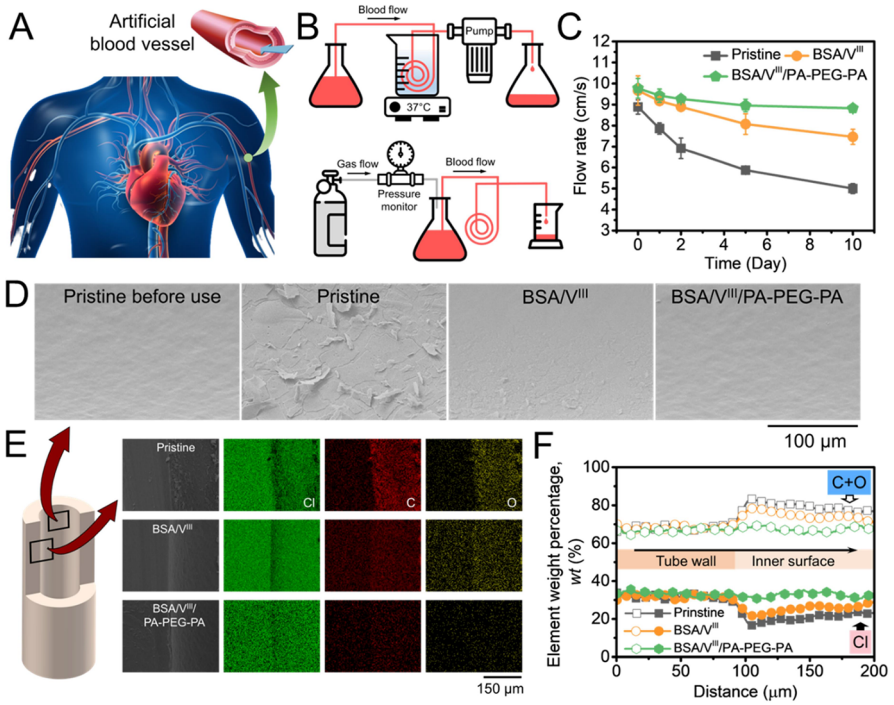

Figure 6. Demonstration of utilizing the BSA/V^{III}/PA−PEG-PA coating for biofouling resistance and surface lubrication in small-diameter artificial blood vessels. (A) Illustration of the vascular grafts for biomedical applications. (B) In vitro blood circulation system. (C) Blood flowing rate in pristine, BSA/V^{III}, and BSA/V^{III}/PA−PEG-PA-coated medical tubes over operation time. (D) Scanning electron microscopy (SEM) characterization of the inner surface of three kinds of medical tubes after 10 days of blood flow. (E) Energy-dispersive spectroscopy (EDS) mapping on the variation of element compositions and (F) line scanning to determine the change of element weight percentage from the tube wall to inner surface of three medical tubes.

decreased flowing rate most likely results from the stubborn adsorption of the biofoulant debris on pristine and BSA/V^{III}-coated inner surfaces, which narrowed down the inner tube and increased the blood drag force. The surface chemistry variation of the pristine, BSA/V^{III}- and BSA/V^{III}/PA−PEG-PA-coated tube surfaces before and after blood circulation was characterized by X-ray photoelectron spectroscopy (XPS) (SI Figures S7 and S8). No N 1s peak was observed on the pristine tube surface before the blood circulation test, whereas strong N 1s peak (C-NH_2, O═C−N−) intensity was detected after the blood circulation test (SI Figures S7A and S8A). The N 1s peak detected on the BSA/V^{III} coated tube before the blood circulation test is mainly due to the BSA proteins. Such N 1s peak intensity, evaluated by the ratio of N to V, obviously increased after the blood circulation test (Figures S7B and S8B). As many biofoulants such as plasma contain N element,[5] the strong C-NH_2, and O═C−N− signals are attributed to the adsorption of biofoulants in blood on pristine and BSA/V^{III} coated tube surfaces. Contrastingly, no obvious change of N 1s peak intensity (ratio of N to V) was observed on the BSA/V^{III}/PA−PEG-PA coated tube before and after the blood circulation test (SI Figures S7C and S8C), implying very minor biofoulants adsorbed on the surface. The antifouling capability, assessed by the XPS test, is consistent with the results of the blood flow rate test and SEM characterization, indicating that the as-prepared coating could effectively prevent biofoulant adsorption in a complex biological fluid.

Considering the utilization of V^{III} ions in the nanocoating preparation, we further evaluated the biocompatibility of the BSA/V^{III}/PA−PEG-PA coating using the human umbilical vein endothelial cells (HUVECs) as the model cell. After 24 and 72 h of incubation, the morphology of 2D HUVEC cell growth was stained using calcein (green) and propidium iodide (red), followed by being visualized in fluorescence microscopy. As shown in Figures S9 and S10, the green fluorescence intensity that identified the incubated live cells on the BSA/V^{III}/PA−PEG-PA coating was comparable with that of the control group and mica, and no significant red fluorescence intensity (stained dead cell) was observed for all three cases. These results indicate the very low toxicity of the BSA/V^{III}/PA−PEG-PA coating, which could be ascribed to the superstrong coordination affinity of V^{III} ions to carboxyl ligands under pH 7.4 (typical pH of biological fluid),[29,30] preventing the dissociation and leakage of V^{III} ions from the coating. Therefore, the potentially toxic effects that might arise from V^{III} leakages should be very limited when the as-developed coating is applied in in vivo applications.

CONCLUSIONS

In summary, we have developed a nanometer-thick bilayer structure that integrates exceptional mechanical strength, lubrication, and antifouling properties as an ultrathin multifunctional coating for miniature bioimplants. The bilayer coating consists of a ∼20 nm BSA protein bottom layer and a ∼5 nm triblock PA−PEG-PA top layer. By employing metal-carboxylate coordination, V^{III} ions serve a dual role: reinforcing the BSA protein network and simultaneously anchoring PEG in a loop conformation. Despite its nanoscale thickness, the BSA layer withstands pressures of up to 10 MPa, while the hydrated PEG layer reduces friction and resists biofouling. Additionally, the V^{III} coordination ensures interlayer integrity, preventing shear-induced failure. Owing to such a synergistic effect of the designed bilayer structure, the as-prepared BSA/

https://doi.org/10.1021/acsnano.4c13800
ACS Nano XXXX, XXX, XXX−XXX

V^{III}/PA−PEG-PA coating demonstrates superlubricity ($\mu \sim 10^{-3}$), superior wear resistance under high contact pressure, and robust antifouling capability against various biofoulants. The application potential of this coating was further demonstrated in a microscale vascular graft, showing long-term stable lubrication and low contamination under human blood pressure in an in vitro circulation test. This work presents a strategic approach to integrating seemingly incompatible properties into ultrathin coatings, providing a customizable platform for multifunctional surfaces in microscale biodevices, such as endovascular microrobots, for biomedical applications.

EXPERIMENTAL SECTION

Materials. All of the chemicals used for polymer synthesis were purchased from Sigma-Aldrich. The phosphate-buffered saline (PBS) used in this work referred to a 150 mM buffer solution of pH 7.4. The macro-RAFT agent (CTA-PEG20K-CTA) was synthesized by attaching the chain transfer agent (S)-1-dodecyl-(S′)- (α,α′-dimethyl-α″-acetic acid) trithiocarbonate to ends of PEG precursors according to the previous reports.[35]

Synthesis of Poly(acrylic acid)-*b*-poly(ethylene glycol)-*b*-poly(acrylic acid) (PA−PEG-PA). Poly(acrylic acid)-*b*-poly(ethylene glycol)-*b*-poly(acrylic acid) (PA−PEG-PA) was synthesized by reversible addition−fragmentation chain transfer (RAFT) polymerization. Briefly, acrylic acid (0.37 g, 2 mmol), CTA-PEG20K-CTA (1.036 g, 0.05 mmol), and N,N′-azobis-(isobutyronitrile) (AIBN) (0.0041 g, 0.025 mmol) were dissolved in 10 mL of 1,4-dioxane. After nitrogen was purged for 20 min, the whole system was allowed to be stirred at 70 °C for 24 h for polymerization. The final reaction mixture was dissolved in 5 mL of dichloromethane and precipitated three times in ethyl ether. The resulting polymer was collected by filtration and vacuum-dried as a white solid powder for further use.

Polymer Characterization. The composition of the resulting polymer was characterized by ^{1}H NMR spectra, which were obtained from a Varian 500 MHz spectrometer at room temperature using D_2O as the solvent. The chemical shifts were reported in parts per million (δ) relative to TMS as the internal reference. The number-average molecular weight (M_n), weight-average molecular weight (M_w), and polydispersity (PDI) of the resulting polymer were determined by a Viscotek conventional gel permeation chromatography (GPC) system equipped with two WAT011545 Waters Ultrahydrogel linear columns using 0.5 mol of sodium acetate/0.5 mol of acetic acid buffer as eluent at a flow rate of 1.0 mL min^{-1} (Table S1).

Preparation of BSA/V^{III}/PA−PEG-PA Coating with the Bilayer Structure. The bilayer BSA/V^{III}/PA−PEG-PA coating was prepared via a facile two-step dip coating method. Mica was utilized as the model surface since it carries a negative surface charge as most bioimplants. Besides, the atomically flat characteristic of the mica surface renders it the ideal substrate for nanoscopic visualization of the morphology change after surface functionalization. First, the surface was immersed in PBS buffer (150 mM, pH 7.4) containing 2 mg/mL bovine serum albumin (BSA) protein for 30 min, followed by thoroughly rinsing with PBS buffer to remove any nonadsorbed BSA protein and gently drying by nitrogen flow, denoting as the BSA bottom layer. Second, the BSA-coated surface was then dipped in PBS buffer (150 mM, pH 7.4) containing 4 mg/mL PA−PEG-PA polymer and 0.1 mg/mL V^{III} ions for 30 min, allowing for the formation of the PA−PEG-PA top layer on the BSA bottom layer through V^{III}-mediated coordination bridging. The obtained bilayer coating was further rinsed with PBS buffer to remove any loosely bound PA−PEG-PA polymer and unbonded V^{III} ions and gently dried with nitrogen flow.

Surface Characterization. Surface morphologies of mica surfaces coated with the BSA bottom layer and BSA/V^{III}/PA−PEG-PA coating were characterized by atomic force microscopy (AFM) imaging (Asylum Research, Santa Barbara, USA). The chemical composition characterization of the as-prepared coatings was obtained using a Kratos Axis 165 X-ray photoelectron spectroscopy (XPS) spectrophotometer (Kratos Analytical, Manchester, UK). A contact angle goniometer (Ossila, UK) was applied to evaluate the water contact angle (WCA) of the BSA/V^{III}/PA−PEG-PA coating formed at a series of introduced-V^{III} concentrations. The surface morphology and element distribution of the pristine, BSA/V^{III}- and BSA/V^{III}/PA−PEG-PA-coated inner wall of small diameter artificial vessels after a blood circulation test were characterized by a field-emission scanning electron microscope (FESEM) (Zeiss Sigma 300 VP-FESEM, Germany) with energy-dispersive X-ray spectroscopy (EDS).

Model Biofoulant Adsorption Test Using Quartz Crystal Microbalance with Dissipation Monitoring (QCM-D). The antifouling ability of the BSA/V^{III}/PA−PEG-PA coating was estimated using a QCM-D (Biolin Scientific, Finland) by quantitatively examining the adsorption and desorption behaviors of three different proteins as the model biofoulants (2 mg/mL in 150 mM PBS buffer, pH 7.4) on bare and BSA/V^{III}/PA−PEG-PA-coated silica sensors. The adsorption of model biofoulants on sensor surfaces would lead to shifts in resonance frequency and energy dissipation curves. The mass of adsorbed model proteins could be determined by fitting the obtained experimental curves using the Voigt viscoelastic model in the QTools software.

Interfacial Interaction Force and Contact Mechanics Measurements Using a Surface Forces Apparatus (SFA). The surface forces apparatus (SFA) was utilized to investigate the interfacial interaction forces between two functionalized surfaces (i.e., BSA-coated surface vs COOH-coated surface, BSA/V^{III}/PA−PEG-PA-coated surface vs BSA/V^{III}/PA−PEG-PA-coated surface and BSA/V^{III}/PA−PEG-PA-coated surface vs model protein-coated surface) under various PBS buffer conditions. The typical experimental setup and working principle of SFA have been reported previously.[56−58] Briefly, two back-silvered mica sheets of 1−5 μm were glued onto a pair of cylindrical silica disks (radius R = 2 cm), respectively. The mica surfaces were treated through surface functionalization to form the testing coatings and then mounted in an SFA chamber in a cross-cylinder configuration. The normal interaction of two cylindrical surfaces of radius R was locally equivalent to that between a sphere of radius R against a flat surface at a separation distance of $D \ll R$ based on the "Derjaguin approximation".[59] The desired testing aqueous solution was then injected between the two surfaces, and the system was allowed to equilibrate for 30 min before force measurements. The surface separation distance D could be monitored in situ and in real-time using the optical interference fringes of equal chromatic order (FECO) by employing the multiple beam interferometry (MBI) optical techniques. The reference distance (D_0 = 0) was determined from an independent measurement of the contact point at which two bare mica surfaces came into contact in the air. The coating thickness D_T could be determined via the shift of the FECO wavelength before and after surface functionalization.

For the normal force measurement, the two surfaces were first brought to approach each other ("approach"), held in contact for a set duration, and then separated ("separation"). The interaction forces were calculated based on the deflection of the cantilever spring supporting the lower disk holder according to Hooke's law. Adhesion force F_{ad} was measured when the two contacted surfaces were detached and jumped apart (so-called "jump out"). The measured adhesion force was related to the adhesion energy per unit area (W_{ad}) based on the Johnson−Kendall−Roberts (JKR) model, where $W_{ad} = 2F_{ad}/3\pi R$.[37,60]

For the frictional force measurement, the lower surface was driven to move laterally relative to the upper surface in reciprocating mode at varying sliding speeds by employing a piezoelectric bimorph slider.[4,61] A micrometer, with its shaft round end located on the end of the single-cantilever spring of the lower surface, facilitated the movement of the lower surface, thereby altering the normal loading F_n between the two surfaces. The disk holder of the upper surface is held by two vertical leaf springs that could bend in the same direction as that of the lower surface. A pair of semiconductor strain gauges attached to

https://doi.org/10.1021/acsnano.4c13800
ACS Nano XXXX, XXX, XXX−XXX

each leaf spring could detect the bending, which is proportional to the friction forces F_s. All friction force measurements were conducted by sliding the lower surface back and forth relative to the top surface at a given normal loading F_n and sliding velocity V_s and over a moving distance of 20 μm. The friction coefficient was calculated using the equation $\mu = F_s/F_n$. The applied normal pressure P was calculated using the equation $P = F_n/A$. The contact area A could be determined through the equation $A = \pi r^2$, in which r, representing the contact radius on mica surfaces, is the half length of the flattened shape of the FECO fringes.

For the contact mechanics test, two BSA-coated or BSA/V^{III}-coated mica surfaces were brought into contact in a PBS buffer. The surface deformation was monitored in real-time by observing the shape of FECO fringes.[62,63] The contact diameter $2r$ was determined from the flat region of the FECO fringes and was varied with increasing applied normal load $F_\perp$ ($2r$ vs $F_\perp$). The loading rate of $dF_\perp/dt$ was kept at 0.6 mN/s, and the maximum load was set at 90 mN.

In-Vitro Blood Circulation Test. The in vitro blood circulation test included two procedures, namely, fetal bovine serum (FBS) circulation and blood flow rate test. In the first procedure, the undiluted FBS was constantly pumped to flow through a small diameter medical tube at 37 °C, and the circulation was maintained at different times. During the first procedure, the biofoulants in FBS would gradually adsorb and accumulate on the inner surface of the medical tube. After circulating for a certain time (i.e., 1, 2, 5, 10 days), the inner surfaces of the fouled tubes were gently washed with PBS buffer followed by setting up for the second procedure. In the second procedure, a constant pressure of 1 MPa (comparable with human blood pressure) was applied to allow FBSto flow through the tubes. The volume of the FBS flowing out of the tube could be obtained from the measuring cylinder placed at the outlet. Considering that the inner diameter of the tube is 0.79 mm, the blood flow rate in medical tubes could then be calculated.

Biocompatibility Test. The biocompatibility of the BSA/V^{III}/PA−PEG-PA coating against human umbilical vein endothelial cells (HUVEC) was evaluated through cytofluorescence staining and green fluorescence intensity, in which blank incubated HUVEC cells as a control. 2D cell culture was conducted by staining the cell nuclei with propidium iodide (PI) and the cytoplasm with calcein. The cells on the surfaces were imaged using laser scanning confocal microscopy (FV3000, OLYMPUS). Five areas were randomly selected for imaging to obtain the average fluorescence intensity.

ASSOCIATED CONTENT

Supporting Information

The Supporting Information is available free of charge at https://pubs.acs.org/doi/10.1021/acsnano.4c13800.

> H^1 NMR spectra of PA−PEG-PA copolymer; calculation of bilayer coating thickness; SFA force measurements between BSA sublayers with/without incorporating V^{III}; cyclic reciprocating friction tests of BSA/V^{III} coatings; XPS spectra of bilayer coating before and after blood circulation; and 2D cell culture and cell staining for biocompatibility evaluation of bilayer coating (PDF)

AUTHOR INFORMATION

Corresponding Authors

Jinyang Jiang − *School of Materials Science and Engineering, Jiangsu Key Laboratory of Construction Materials, Southeast University, Nanjing 211189, People's Republic of China;* orcid.org/0000-0002-0134-9373; Email: jiangjinyang16@163.com

Jiawen Zhang − *Department of Chemical and Materials Engineering, University of Alberta, Edmonton, Alberta T6G 1H9, Canada; School of Materials Science and Engineering, Jiangsu Key Laboratory of Construction Materials, Southeast University, Nanjing 211189, People's Republic of China;* orcid.org/0000-0003-3004-5536; Email: jwzhang@seu.edu.cn

Hongbo Zeng − *Department of Chemical and Materials Engineering, University of Alberta, Edmonton, Alberta T6G 1H9, Canada;* orcid.org/0000-0002-1432-5979; Email: hongbo.zeng@ualberta.ca

Authors

Li Xiang − *School of Mechanical Engineering, Jiangsu Key Laboratory for Design and Manufacture of Micro-Nano Biomedical Instruments, Southeast University, Nanjing 211189, People's Republic of China; Department of Chemical and Materials Engineering, University of Alberta, Edmonton, Alberta T6G 1H9, Canada;* orcid.org/0000-0003-1154-2502

Yuhao Zhang − *School of Mechanical Engineering, Jiangsu Key Laboratory for Design and Manufacture of Micro-Nano Biomedical Instruments, Southeast University, Nanjing 211189, People's Republic of China*

Ziqian Zhao − *Department of Chemical and Materials Engineering, University of Alberta, Edmonton, Alberta T6G 1H9, Canada;* orcid.org/0000-0003-3380-2803

Yi Tao − *School of Mechanical Engineering, Jiangsu Key Laboratory for Design and Manufacture of Micro-Nano Biomedical Instruments, Southeast University, Nanjing 211189, People's Republic of China*

Wenda Wang − *Department of Chemical and Materials Engineering, University of Alberta, Edmonton, Alberta T6G 1H9, Canada;* orcid.org/0000-0002-7101-8967

Jifang Liu − *Cancer Center, The Fifth Affiliated Hospital, Guangzhou Medical University, Guangzhou 510700, People's Republic of China*

Yunfei Chen − *School of Mechanical Engineering, Jiangsu Key Laboratory for Design and Manufacture of Micro-Nano Biomedical Instruments, Southeast University, Nanjing 211189, People's Republic of China;* orcid.org/0000-0002-8682-868X

Complete contact information is available at: https://pubs.acs.org/10.1021/acsnano.4c13800

Author Contributions

The manuscript was written through contributions of all authors. All authors have given approval to the final version of the manuscript.

Notes

The authors declare no competing financial interest.

ACKNOWLEDGMENTS

The authors thank the financial support from the National Natural Science Foundation of China (Grant No. 52108195 and No. 52305185), the Natural Science Foundation of Jiangsu Province (Grants No. BK20220835 and No. BK20210264), the Jiangsu Provincial Double-Innovation Doctor Program (Grant No. JSSCBS20220160), the Nanjing Overseas Educated Personnel Science and Technology Innovation Program (Class A) and the Fundamental Research Funds for the Central Universities (Grant No. 2242022R10174), the National Sciences and Engineering Research Council of Canada (NSERC), the Canada Foundation for Innovation (CFI), and the Canada Research Chairs Program.

REFERENCES

(1) Yuk, H.; Wu, J.; Zhao, X. Hydrogel Interfaces for Merging Humans and Machines. *Nat. Rev. Mater.* **2022**, *7* (12), 935−952.
(2) Yu, Y.; Yuk, H.; Parada, G. A.; Wu, Y.; Liu, X.; Nabzdyk, C. S.; Youcef-Toumi, K.; Zang, J.; Zhao, X. Multifunctional "Hydrogel Skins" on Diverse Polymers with Arbitrary Shapes. *Adv. Mater.* **2019**, *31* (7), No. 1807101.
(3) Wang, Y.; Sun, Y.; Avestro, A.-J.; McGonigal, P. R.; Zhang, H. Supramolecular Repair of Hydration Lubrication Surfaces. *Chem.* **2022**, *8* (2), 480−493.
(4) Xiang, L.; Zhang, J.; Wang, W.; Wei, Z.; Chen, Y.; Zeng, H. Targeted Repair of Super-Lubricating Surfaces Via Pairing Click Chemistry. *Adv. Funct. Mater.* **2023**, *33* (31), No. 2301593.
(5) Zhao, Z.; Pan, M.; Qiao, C.; Xiang, L.; Liu, X.; Yang, W.; Chen, X.-Z.; Zeng, H. Bionic Engineered Protein Coating Boosting Anti-Biofouling in Complex Biological Fluids. *Adv. Mater.* **2023**, *35* (6), No. 2208824.
(6) Del Rio, J. S.; Henry, O. Y. F.; Jolly, P.; Ingber, D. E. An Antifouling Coating That Enables Affinity-Based Electrochemical Biosensing in Complex Biological Fluids. *Nat. Nanotechnol.* **2019**, *14* (12), 1143−1149.
(7) Kang, T.; Banquy, X.; Heo, J.; Lim, C.; Lynd, N. A.; Lundberg, P.; Oh, D. X.; Lee, H.-K.; Hong, Y.-K.; Hwang, D. S.; Waite, J. H.; Israelachvili, J. N.; Hawker, C. J. Mussel-Inspired Anchoring of Polymer Loops That Provide Superior Surface Lubrication and Antifouling Properties. *ACS Nano* **2016**, *10* (1), 930−937.
(8) Gunawan, S. T.; Kempe, K.; Bonnard, T.; Cui, J.; Alt, K.; Law, L. S.; Wang, X.; Westein, E.; Such, G. K.; Peter, K.; Hagemeyer, C. E.; Caruso, F. Multifunctional Thrombin-Activatable Polymer Capsules for Specific Targeting to Activated Platelets. *Adv. Mater.* **2015**, *27* (35), 5153−5157.
(9) Mu, D.; Wang, W.; Li, J.; Lv, P.; Liu, R.; Tan, Y.; Zhong, C.; Qi, Y.; Sun, X.; Liu, Y.; Shen, S.; Li, Y.; Xu, B.; Zhang, B. Ultrasmall Fe(III)-Tannic Acid Nanoparticles to Prevent Progression of Atherosclerotic Plaques. *ACS Appl. Mater. Interfaces* **2021**, *13* (29), 33915−33925.
(10) Magin, C. M.; Cooper, S. P.; Brennan, A. B. Non-Toxic Antifouling Strategies. *Mater. Today* **2010**, *13* (4), 36−44.
(11) Li, S.; Bai, Y.; Liu, X.; Zhang, Y.; Tang, Y.; Zhao, F.; Li, Q.; Guo, Z.; Feng, Z.; Dong, A.; Kong, D.; Wang, W.; Huang, P. Bio-Inspired Robust, Superhydrophilic and Superlubric Artificial Vascular Endothelium Coating for Anti-Thromboinflammation on Blood-Contacting Devices. *Compos. B. Eng.* **2023**, *257*, No. 110670.
(12) Fleischer, S.; Tavakol, D. N.; Vunjak-Novakovic, G. From Arteries to Capillaries: Approaches to Engineering Human Vasculature. *Adv. Funct. Mater.* **2020**, *30* (37), No. 1910811.
(13) Lin, W.; Klein, J. Hydration Lubrication in Biomedical Applications: From Cartilage to Hydrogels. *Acc. Mater. Res.* **2022**, *3* (2), 213−223.
(14) Ma, S.; Zhang, X.; Yu, B.; Zhou, F. Brushing up Functional Materials. *NPG Asia Mater.* **2019**, *11*, 24.
(15) Miller Naranjo, B.; Zollo, M.; Sieber, S. A.; Lieleg, O. Lubricity, Wear Prevention, and Anti-Biofouling Properties of Macromolecular Coatings for Endotracheal Tubes. *Biomater. Sci.* **2024**, *12* (5), 1228−1238.
(16) Morgese, G.; Cavalli, E.; Rosenboom, J.-G.; Zenobi-Wong, M.; Benetti, E. M. Cyclic Polymer Grafts That Lubricate and Protect Damaged Cartilage. *Angew. Chem., Int. Ed.* **2018**, *57* (6), 1621−1626.
(17) Kim, J.; Zhang, G.; Shi, M.; Suo, Z. Fracture, Fatigue, and Friction of Polymers in Which Entanglements Greatly Outnumber Cross-Links. *Science* **2021**, *374* (6564), 212−216.
(18) Yang, J.; Bai, R.; Chen, B.; Suo, Z. Hydrogel Adhesion: A Supramolecular Synergy of Chemistry, Topology, and Mechanics. *Adv. Funct. Mater.* **2020**, *30* (2), No. 1901693.
(19) Gong, J. P.; Osada, Y. Soft and Wet Materials: From Hydrogels to Biotissues. In *High Solid Dispersions*; Springer, 2010; *236*, 203−246.
(20) Zhang, C.; Wu, B.; Zhou, Y.; Zhou, F.; Liu, W.; Wang, Z. Mussel-Inspired Hydrogels: From Design Principles to Promising Applications. *Chem. Soc. Rev.* **2020**, *49* (11), 3605−3637.
(21) Lee, B. P.; Messersmith, P. B.; Israelachvili, J. N.; Waite, J. H. Mussel-Inspired Adhesives and Coatings. *Ann. Rev. Mater. Res.* **2011**, *41*, 99−132.
(22) Zeng, H.; Hwang, D. S.; Israelachvili, J. N.; Waite, J. H. Strong Reversible Fe^{3+}-Mediated Bridging between Dopa-Containing Protein Films in Water. *Proc. Natl. Acad. Sci. U.S.A.* **2010**, *107* (29), 12850−12853.
(23) Faghihnejad, A.; Zeng, H. *Polymer Adhesion, Friction, and Lubrication*; Wiley, 2013.
(24) Qu, M.; Liu, H.; Yan, C.; Ma, S.; Cai, M.; Ma, Z.; Zhou, F. Layered Hydrogel with Controllable Surface Dissociation for Durable Lubrication. *Chem. Mater.* **2020**, *32* (18), 7805−7813.
(25) Rong, M.; Liu, H.; Scaraggi, M.; Bai, Y.; Bao, L.; Ma, S.; Ma, Z.; Cai, M.; Dini, D.; Zhou, F. High Lubricity Meets Load Capacity: Cartilage Mimicking Bilayer Structure by Brushing up Stiff Hydrogels from Subsurface. *Adv. Funct. Mater.* **2020**, *30* (39), No. 2004062.
(26) Wang, R.; Wei, Q.; Sheng, W.; Yu, B.; Zhou, F.; Li, B. Driving Polymer Brushes from Synthesis to Functioning. *Angew. Chem., Int. Ed.* **2023**, *62* (27), No. e202219312.
(27) Li, M.-X.; Wei, Q.-Q.; Mo, H.-L.; Ren, Y.; Zhang, W.; Lu, H.-J.; Joung, Y. K. Challenges and Advances in Materials and Fabrication Technologies of Small-Diameter Vascular Grafts. *Biomater. Res.* **2023**, *27* (1), 58.
(28) Tanaka, T.; Abe, Y.; Cheng, C.-J.; Tanaka, R.; Naito, A.; Asakura, T. Development of Small-Diameter Elastin-Silk Fibroin Vascular Grafts. *Front. Bioeng. Biotechnol.* **2021**, *8*, No. 622220.
(29) Mesko, M.; Xiang, L.; Bohle, S.; Hwang, D. S.; Zeng, H.; Harrington, M. J. Catechol-Vanadium Binding Enhances Cross-Linking and Mechanics of a Mussel Byssus Coating Protein. *Chem. Mater.* **2021**, *33* (16), 6530−6540.
(30) Priemel, T.; Palia, G.; Foerste, F.; Jehle, F.; Sviben, S.; Mantouvalou, I.; Zaslansky, P.; Bertinetti, L.; Harrington, M. J. Microfluidic-Like Fabrication of Metal Ion-Cured Bioadhesives by Mussels. *Science* **2021**, *374* (6564), 206−211.
(31) Hu, X.; Tian, J.; Li, C.; Su, H.; Qin, R.; Wang, Y.; Cao, X.; Yang, P. Amyloid-Like Protein Aggregates: A New Class of Bioinspired Materials Merging an Interfacial Anchor with Antifouling. *Adv. Mater.* **2020**, *32* (23), No. 2000128.
(32) Claesson, P. M.; Blomberg, E.; Froberg, J. C.; Nylander, T.; Arnebrant, T. Protein Interactions at Solid-Surfaces. *Adv. Colloid Interface Sci.* **1995**, *57*, 161−227.
(33) Rehder, D. The Coordination Chemistry of Vanadium as Related to Its Biological Functions. *Coord. Chem. Rev.* **1999**, *182*, 297−322.
(34) Pessoa, J. C.; Santos, M. F. A.; Correia, I.; Sanna, D.; Sciortino, G.; Garribba, E. Binding of Vanadium Ions and Complexes to Proteins and Enzymes in Aqueous Solution. *Coord. Chem. Rev.* **2021**, *449*, No. 214192.
(35) Wang, W.; Zeng, Z.; Xiang, L.; Liu, C.; Diaz-Dussan, D.; Du, Z.; Asha, A. B.; Yang, W.; Peng, Y.-Y.; Pan, M.; Narain, R.; Liu, J.; Zeng, H. Injectable Self-Healing Hydrogel Via Biological Environment-Adaptive Supramolecular Assembly for Gastric Perforation Healing. *ACS Nano* **2021**, *15* (6), 9913−9923.
(36) Xiang, L.; Zhu, S.; Li, M.; Zhang, J.; El-Din, M. G.; Zeng, H. Probing Fouling Mechanism of Naphthenic Acids on Forward Osmosis Polymer Membranes in Oil Sands Process Water Treatment. *J. Membr. Sci.* **2019**, *576*, 161−170.
(37) Israelachvili, J. N. *Intermolecular and Surface Forces (Third ed.)*; Academic Press: Boston, 2011.
(38) Yang, W.; Zhao, Z.; Pan, M.; Gong, L.; Wua, F.; Huang, C.; Wang, X.; Wang, J.; Zeng, H. Mussel-Inspired Polyethylene Glycol Coating for Constructing Antifouling Membrane for Water Purification. *J. Colloid Interface Sci.* **2022**, *625*, 628−639.
(39) Zhao, Z.; Pan, M.; Yang, W.; Huang, C.; Qiao, C.; Yang, H.; Wang, J.; Wang, X.; Liu, J.; Zeng, H. Bioinspired Engineered Proteins Enable Universal Anchoring Strategy for Surface Functionalization. *J. Colloid Interface Sci.* **2023**, *650*, 1525−1535.
(40) Zeng, H.; Huang, J.; Tian, Y.; Li, L.; Tirrell, M. V.; Israelachvili, J. N. Adhesion and Detachment Mechanisms between Polymer and

https://doi.org/10.1021/acsnano.4c13800
ACS Nano XXXX, XXX, XXX−XXX

Solid Substrate Surfaces: Using Polystyrene-Mica as a Model System. *Macromolecules* **2016**, *49* (14), 5223−5231.
(41) Chen, J.; Peng, Q.; Peng, X.; Zhang, H.; Zeng, H. Probing and Manipulating Noncovalent Interactions in Functional Polymeric Systems. *Chem. Rev.* **2022**, *122* (18), 14594−14678.
(42) Li, L.; Yan, B.; Zhang, L.; Tian, Y.; Zeng, H. Mussel-Inspired Antifouling Coatings Bearing Polymer Loops. *Chem. Commun.* **2015**, *51* (87), 15780−15783.
(43) Lin, W.; Kluzek, M.; Iuster, N.; Shimoni, E.; Kampf, N.; Goldberg, R.; Klein, J. Cartilage-Inspired, Lipid-Based Boundary-Lubricated Hydrogels. *Science* **2020**, *370* (6514), 335−338.
(44) Wang, B.; Tirado, A.; Yang, F.; Moran, C.; Vander Woude, M.; Song, Y.; Wang, X.; Qiao, R.; Bai, S.; Guo, Q.; Tang, H.; Li, L. A Functionalized Ionic Liquid as the Next-Generation Nano-Lubricant. *Droplet* **2022**, *1* (2), 192−201.
(45) Fogelson, A. L.; Neeves, K. B. Fluid Mechanics of Blood Clot Formation. *Ann. Rev. Fluid Mech.* **2015**, *47*, 377−403.
(46) Chapman, G. B.; Cokelet, G. R. Flow Resistance and Drag Forces Due to Multiple Adherent Leukocytes in Postcapillary Vessels. *Biophys. J.* **1998**, *74* (6), 3292−3301.
(47) Jiang, C.; Wang, G.; Hein, R.; Liu, N.; Luo, X.; Davis, J. J. Antifouling Strategies for Selective in Vitro and in Vivo Sensing. *Chem. Rev.* **2020**, *120* (8), 3852−3889.
(48) Huang, H.; Zhang, C.; Crisci, R.; Lu, T.; Hung, H.-C.; Sajib, M. S. J.; Sarker, P.; Ma, J.; Wei, T.; Jiang, S.; Chen, Z. Strong Surface Hydration and Salt Resistant Mechanism of a New Nonfouling Zwitterionic Polymer Based on Protein Stabilizer Tmao. *J. Am. Chem. Soc.* **2021**, *143* (40), 16786−16795.
(49) Xia, Y.; Adibnia, V.; Huang, R.; Murschel, F.; Faivre, J.; Xie, G.; Olszewski, M.; De Crescenzo, G.; Qi, W.; He, Z.; Su, R.; Matyjaszewski, K.; Banquy, X. Biomimetic Bottlebrush Polymer Coatings for Fabrication of Ultralow Fouling Surfaces. *Angew. Chem., Int. Ed.* **2019**, *58* (5), 1308−1314.
(50) Li, Q.; Wen, C.; Yang, J.; Zhou, X.; Zhu, Y.; Zheng, J.; Cheng, G.; Bai, J.; Xu, T.; Ji, J.; Jiang, S.; Zhang, L.; Zhang, P. Zwitterionic Biomaterials. *Chem. Rev.* **2022**, *122* (23), 17073−17154.
(51) Zander, Z. K.; Becker, M. L. Antimicrobial and Antifouling Strategies for Polymeric Medical Devices. *ACS Macro Lett.* **2018**, *7* (1), 16−25.
(52) Obiweluozor, F. O.; Emechebe, G. A.; Kim, D.-W.; Cho, H.-J.; Park, C. H.; Kim, C. S.; Jeong, I. S. Considerations in the Development of Small-Diameter Vascular Graft as an Alternative for Bypass and Reconstructive Surgeries: A Review. *Cardiovasc. Eng. Technol.* **2020**, *11* (5), 495−521.
(53) Dimitrievska, S.; Wang, J.; Lin, T.; Weyers, A.; Bai, H.; Qin, L.; Li, G.; Cai, C.; Kypson, A.; Kristofik, N.; Gard, A.; Sundaram, S.; Yamamoto, K.; Wu, W.; Zhao, L.; Kural, M. H.; Yuan, Y.; Madri, J.; Kyriakides, T. R.; Linhardt, R. J.; Niklason, L. E. Glycocalyx-Like Hydrogel Coatings for Small Diameter Vascular Grafts. *Adv. Funct. Mater.* **2020**, *30* (23), No. 1908963.
(54) Zheng, W.; Liu, M.; Qi, H.; Wen, C.; Zhang, C.; Mi, J.; Zhou, X.; Zhang, L.; Fan, D. Mussel-Inspired Triblock Functional Protein Coating with Endothelial Cell Selectivity for Endothelialization. *J. Colloid Interface Sci.* **2020**, *576*, 68−78.
(55) Badv, M.; Bayat, F.; Weitz, J. I.; Didar, T. F. Single and Multi-Functional Coating Strategies for Enhancing the Biocompatibility and Tissue Integration of Blood-Contacting Medical Implants. *Biomaterials* **2020**, *258*, No. 120291.
(56) Israelachvili, J.; Min, Y.; Akbulut, M.; Alig, A.; Carver, G.; Greene, W.; Kristiansen, K.; Meyer, E.; Pesika, N.; Rosenberg, K.; Zeng, H. Recent Advances in the Surface Forces Apparatus (SfA) Technique. *Rep. Prog. Phys.* **2010**, *73* (3), No. 036601.
(57) Zhang, J.; Xiang, L.; Yan, B.; Zeng, H. Nanomechanics of Anion-Π Interaction in Aqueous Solution. *J. Am. Chem. Soc.* **2020**, *142* (4), 1710−1714.
(58) Zeng, H.; Kristiansen, K.; Wang, P.; Bergli, J.; Israelachvili, J. Surface-Induced Patterns from Evaporating Droplets of Aqueous Carbon Nanotube Dispersions. *Langmuir* **2011**, *27* (11), 7163−7167.
(59) Johnson, K. L.; Kendall, K.; Roberts, A. D. Surface Energy and Contact of Elastic Solids. *Proc. R. Soc. A Math. Phys. Eng. Sci.* **1971**, *324* (1558), 301−313.
(60) Xiang, L.; Zhang, J.; Wang, W.; Gong, L.; Zhang, L.; Yan, B.; Zeng, H. Nanomechanics of Π-Cation-Π Interaction with Implications for Bio-Inspired Wet Adhesion. *Acta Biomater.* **2020**, *117*, 294−301.
(61) Kristiansen, K.; Zeng, H.; Wang, P.; Israelachvili, J. N. Microtribology of Aqueous Carbon Nanotube Dispersions. *Adv. Funct. Mater.* **2011**, *21* (23), 4555−4564.
(62) Gong, L.; Xiang, L.; Zhang, J.; Chen, J.; Zeng, H. Fundamentals and Advances in the Adhesion of Polymer Surfaces and Thin Films. *Langmuir* **2019**, *35* (48), 15914−15936.
(63) Xiang, L.; Zhang, J.; Gong, L.; Zeng, H. Surface Forces and Interaction Mechanisms of Soft Thin Films under Confinement: A Short Review. *Soft Matter* **2020**, *16* (29), 6697−6719.

https://doi.org/10.1021/acsnano.4c13800
ACS Nano XXXX, XXX, XXX−XXX